Sensors and Materials, Vol. 37, No. 7 (2025) 3051–3060
MYU Tokyo

S & M 4102

Photoluminescence and Magnetic Properties of Co/Ca-codoped ZnO Nanowires Prepared by Hydrothermal Method

Ming-Cheng Kao,[1*] Kai-Huang Chen,[2] Jun-Hong Weng,[3] and Chih-Hung Chiang[4]

[1]Graduate Institute of Aeronautics, Department of Information and Communication Engineering, Chaoyang University of Technology, Taichung 413310, Taiwan
[2]Department of Electronic Engineering, Cheng Shiu University, Kaohsiung 83347, Taiwan
[3]Department of Electronic Engineering, National Formosa University, Yunlin 632, Taiwan
[4]Graduate Institute of Aeronautics, Chaoyang University of Technology, Taichung 413310, Taiwan

(Received November 10, 2024; accepted June 16, 2025)

Keywords: nanowire, ZnO, Co/Ca codoping, magnetization

In this study, a ZnO seed layers was fabricated on a silicon substrate by a sol–gel method, and vertically aligned Co/Ca-codoped ZnO (CCZ) nanowire arrays were prepared on the ZnO seed layer by a hydrothermal method. The Co and Ca were doped to improve the structural, photoluminescence, and magnetic properties of CCZ nanowire arrays. The CCZ and undoped ZnO nanowires exhibited the c-axis orientation and single polycrystalline phase with the wurtzite hexagonal structure of P63/mc. The photoluminescence spectrum showed that the UV emission (about 374 nm) of the CCZ nanowires decreased and the green light emission (about 513 nm) increased compared with those of undoped ZnO nanowires. From the hysteresis curve, the magnetic field dependence of the magnetization as a function of magnetic field showed the existence of ferromagnetism for CCZ and undoped ZnO nanowires. The saturation magnetization of the CCZ nanowires is 0.46 emu/g, which is better than that of undoped ZnO nanowires (0.22 emu/g). These results demonstrate the properties of CCZ nanowire arrays with potential applications in optoelectronics and spintronics.

1. Introduction

Zinc oxide (ZnO) is a wide-bandgap semiconductor with a bandgap of 3.37 eV and a high exciton binding energy of 60 meV, which makes it suitable for various optoelectronic and spintronic applications.[1–3] Owing to its unique electrical, optical, and chemical properties, ZnO has been extensively investigated and has shown great promise in applications such as ultraviolet (UV) photodetectors, gas sensors, piezoelectric devices, and transparent conductive oxides.[4,5] Compared with other semiconductor materials, ZnO is known for its chemical stability, nontoxicity, and abundance, which have further driven interest in its use for advanced electronic and optoelectronic devices. ZnO nanowires have attracted significant attention because of their high aspect ratio, superior electronic transport properties, and enhanced surface-to-volume ratio.[6–8] These unique features make ZnO nanowires advantageous for nanoscale devices,

*Corresponding author: e-mail: kmc@cyut.edu.tw
https://doi.org/10.18494/SAM5627

ISSN 0914-4935
https://myukk.org/

including photodetectors, field-effect transistors, and nanosensors.[9,10] To further enhance the functional properties of ZnO nanowires, doping has been widely employed to modulate their electrical, magnetic, and optical characteristics.[11–16] Through the incorporation of dopants into the ZnO lattice, their intrinsic properties such as carrier concentration, defect states, and magnetic moments can be effectively altered, allowing for improved device performance.

Transition metal (TM) doping, including elements such as Co, Mn, Ni, and Fe, has been extensively studied for ZnO owing to its potential to induce room-temperature ferromagnetism, which is crucial for spintronic applications.[17–19] The introduction of these dopants can create localized magnetic moments and, under appropriate conditions, lead to long-range magnetic ordering. In addition, it has been reported that nonmagnetic elements such as Ca, Mg, and Al can also be used to modify the defect structure and optical properties of ZnO, thereby enhancing its photoluminescence and conductivity.[20–22] Although extensive research has been conducted on TM-doped ZnO, relatively few studies have focused on the codoping of ZnO nanowires with both magnetic and nonmagnetic elements. Among the various codoping strategies, the combination of Co and Ca is expected to offer unique advantages. Co doping is known to introduce localized magnetic moments in ZnO, whereas Ca doping has been reported to modulate the defect density and carrier concentration, which can affect both optical and electrical properties.[23–25] In this study, Co/Ca-codoped ZnO (CCZ) nanowires were fabricated by the hydrothermal method. The structural, photoluminescence, and magnetic properties of the CCZ nanowires were systematically investigated to determine the impact of dual doping on the multifunctional characteristics of the nanowires.

2. Materials and Methods

A ZnO seed layer was prepared on a silicon substrate by the sol–gel method, which is a chemical process for synthesizing materials by converting a liquid solution into a solid gel. This process involves hydrolysis and condensation steps. Hydrolysis is the reaction of a precursor molecule with water to form hydroxyl groups. Condensation is the combination of hydroxyl groups to form metal–oxygen–metal bonds to form a network structure. This sol–gel method has the advantages of using simple equipment and precise control of material thickness at low temperatures. The sol–gel precursor solution was prepared by dissolving 0.1 M zinc acetate dihydrate [$Zn(CH_3COO)_2{\cdot}2H_2O$, Sigma-Aldrich, 99.5% purity] in 30 mL of ethanol (C_2H_5OH, Merck, 99.9% purity) under magnetic stirring at room temperature for 30 min. To stabilize the solution, monoethanolamine (MEA, C_2H_7NO, Sigma-Aldrich, 99% purity) was added dropwise at a molar MEA-to-zinc acetate ratio of 1:1. The resulting solution was stirred continuously for 1 h until a clear and homogeneous sol was formed. Before spin coating, the sol–gel solution was subjected to differential thermal analysis (DTA) and thermogravimetric analysis (TGA) using a DTA-TGA analyzer (TA Instruments SDT Q600) to study the thermal stability and phase transitions of the precursor. Silicon substrates were cleaned sequentially using acetone, ethanol, and deionized water in an ultrasonic bath for 10 min each and then dried under nitrogen gas. The prepared ZnO sol–gel solution was spin-coated onto the cleaned silicon substrates at 3000 rpm for 30 s using a spin coater (Laurell WS-400B-6NPP). The coating process was repeated three

times to obtain a uniform seed layer. After each coating cycle, the substrates were preheated at 300 ℃ for 10 min to evaporate the solvent and then annealed at 600 ℃ for 1 h in a muffle furnace (Lindberg/Blue M, Thermo Scientific) under a nitrogen atmosphere to crystallize the ZnO seed layer.

CCZ nanowire arrays were prepared on the ZnO seed layer by a hydrothermal method. The hydrothermal solution was prepared by dissolving 0.05 M zinc nitrate hexahydrate [$Zn(NO_3)_2{\cdot}6H_2O$, Sigma-Aldrich, 98% purity] and 0.05 M hexamethylenetetramine (HMTA, $C_6H_{12}N_4$, Sigma-Aldrich, 99% purity) in 100 mL of deionized water under constant stirring. Cobalt nitrate hexahydrate [$Co(NO_3)_2{\cdot}6H_2O$, Alfa Aesar, 99% purity] and calcium nitrate tetrahydrate [$Ca(NO_3)_2{\cdot}4H_2O$, Alfa, 99% purity] were used as dopant sources and added to the solution at appropriate molar concentrations to achieve the desired Co and Ca doping levels. The molar ratios of Co and Ca to Zn were both fixed at 3 at%. The prepared solution was transferred to an autoclave, and the ZnO seed layer was placed upside-down in the solution to facilitate the uniform growth of nanowires. The autoclave was then sealed and maintained at 90 ℃ for 6 h. The surface morphology and microstructure of the nanowire arrays were characterized by field-emission scanning electron microscopy (FE-SEM, JEOL JSM-6500F). The crystalline structure was analyzed by X-ray diffraction (XRD, Bruker D8 Advance) with Cu Kα radiation (λ = 1.5406 Å). The 2θ scan range for the measurement was from 20° to 60°. The step angle was configured at 0.02° with a scan rate of 1°/min. The photoluminescence properties were investigated using a fluorescence spectrometer (Horiba Fluoromax-4) with a 325 nm He–Cd laser as the excitation source. Magnetic measurements were performed at room temperature using a vibrating sample magnetometer (VSM, Lakeshore 7400) in a measurement magnetic field range of ±2 Tesla. Thermal analysis was performed by TGA and differential scanning calorimetry (DSC) using a TA Instruments Q50 TGA and a TA Instruments Q2000 DSC, respectively.

3. Results and Discussion

3.1 Thermal analysis

DTA and TGA were performed to investigate the thermal stability and phase transition behavior of the ZnO precursor solution. Figure 1 shows the TGA/DTA curves from room temperature to 600 ℃, with the TGA curve displaying weight loss as a function of temperature. The initial weight loss observed below 150 ℃ corresponds to the evaporation of solvents and water molecules in the solution, indicating the removal of solvents and the decomposition of low-boiling-point organic components. The second stage of weight loss, occurring between 150 and 300 ℃, can be attributed to the thermal decomposition of the zinc acetate precursor and MEA, which was used as a stabilizer in the sol–gel process. Between 300 and 500 ℃, a significant weight loss of approximately 10% was recorded, indicating the complete decomposition of the zinc acetate complex and its conversion to ZnO. The final residual mass after 600 ℃ was approximately 40%. In DTA, an exothermic peak around 300 ℃ is observed, likely due to the further decomposition of zinc acetate complexes and the combustion of organic residues. Another prominent exothermic peak around 600 ℃ signifies the crystallization of ZnO,

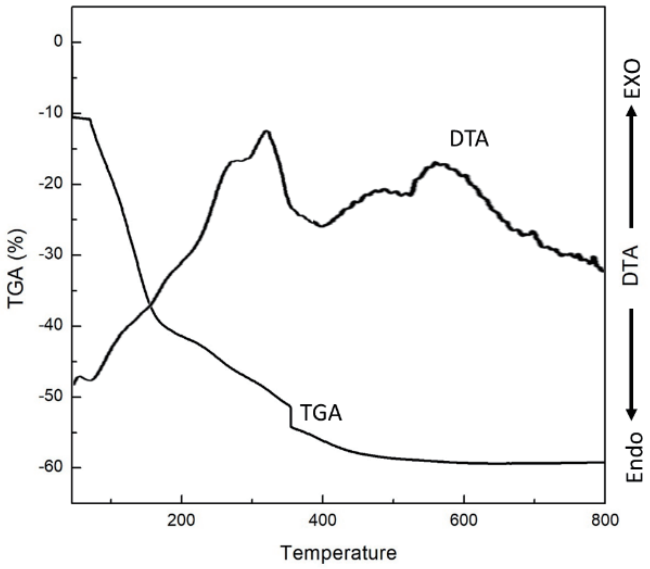

Fig. 1. DTA and TGA results for ZnO precursor solution.

confirming the phase transition and complete crystallization of ZnO. These results indicate that 600 °C is the optimal temperature for obtaining a stable ZnO crystal structure, which supports the choice of this temperature for the rapid thermal annealing (RTA) step in the fabrication process to enhance the crystallinity of the ZnO seed layer.

3.2 Structural analysis

The crystalline structure and phase composition of the synthesized CCZ nanowire arrays were investigated by XRD. The obtained XRD patterns are shown in Fig. 2, displaying distinct diffraction peaks corresponding to the wurtzite hexagonal ZnO phase (JCPDS No. 36-1451). The major diffraction peaks observed at 2θ values of 34.4° can be indexed to the (002) planes, which is characteristic of the hexagonal wurtzite structure. The peak at 34.4° indicates a strong c-axis orientation of the ZnO nanowires, suggesting that the growth is predominantly in the [002] direction. It was observed that the (002) peak position of the CCZ nanowires shifted to a slightly lower 2θ angle by approximately 0.04°, as shown in Fig. 3. To calculate the lattice constant c for the hexagonal wurtzite structure, we can use the general formula for the interplanar spacing d_{hkl}:

$$\frac{1}{d_{hkl}^2} = \frac{4}{3}\left(\frac{h^2 + hk + k^2}{a^2}\right) + \frac{l^2}{c^2}, \tag{1}$$

where h, k, and l are the Miller indices, a and c are lattice constants, and d_{hkl} is the interplanar spacing for the (hkl) planes. The lattice constant 'c' is obtained through the relation $c = (\lambda/\sin\theta)$ for the plane (002). The calculated values of lattice constant 'c' for the undoped ZnO and CCZ nanowires were 0.520 and 0.527 nm, respectively. This increased lattice constant for the CCZ

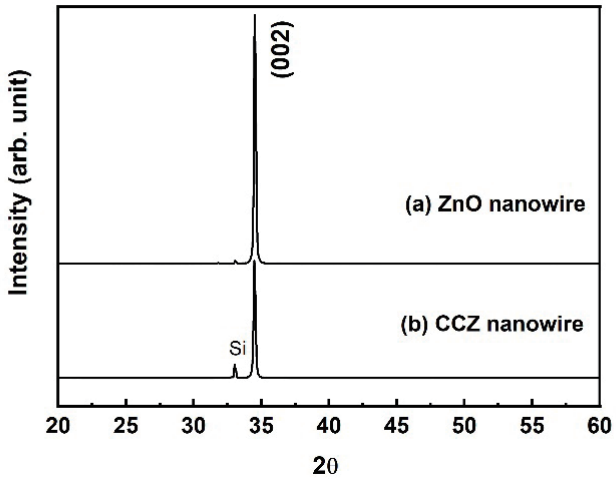

Fig. 2. XRD patterns of (a) ZnO nanowires and (b) CCZ nanowires.

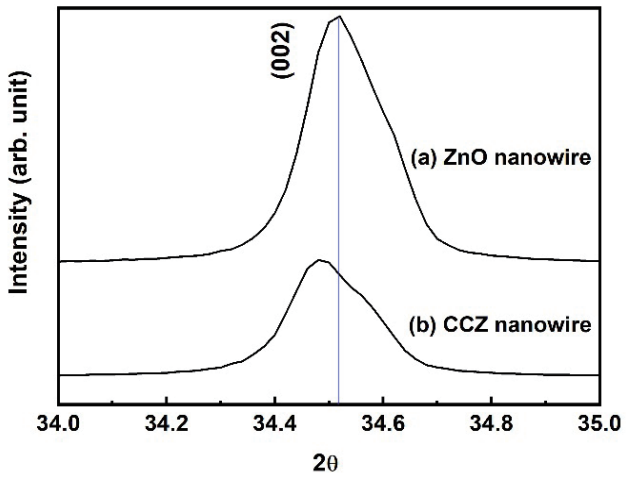

Fig. 3. Enlarged view of XRD peaks in 2θ range of 34°–35° for (002) plane of (a) ZnO nanowires and (b) CCZ nanowires.

nanowires is due to the incorporation of Co and Ca ions into the ZnO lattice. The larger Ca^{2+} ions (ionic radius = 0.100 nm) replace Zn^{2+} ions (ionic radius = 0.074 nm) in the crystal structure, resulting in a localized strain and lattice distortion. The larger Ca^{2+} ions exert a more dominant effect, leading to an overall increase in the lattice parameter, which causes the diffraction peak to move to a lower angle.[26]

3.3 Morphological analysis

The surface morphologies of undoped ZnO nanowires and CCZ nanowires were analyzed by SEM. The top-view SEM image is shown in Fig. 4. The undoped ZnO nanowires exhibit a clear hexagonal cross-sectional shape, which is characteristic of the ZnO wurtzite crystal structure in Fig. 4(a). The hexagonal morphology shows that the nanowires grow mainly along the *c*-axis,

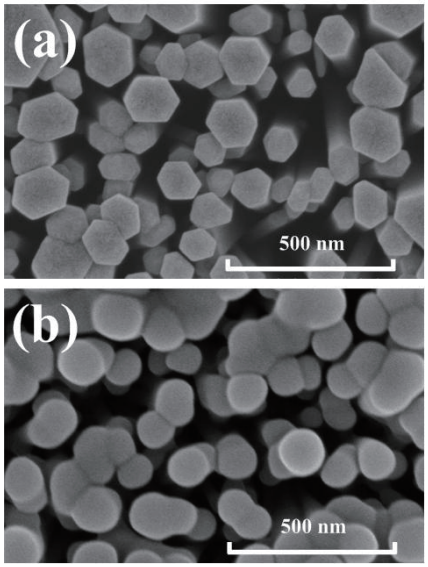

Fig. 4. Top-view SEM images of (a) undoped ZnO nanowire and (b) CCZ nanowire.

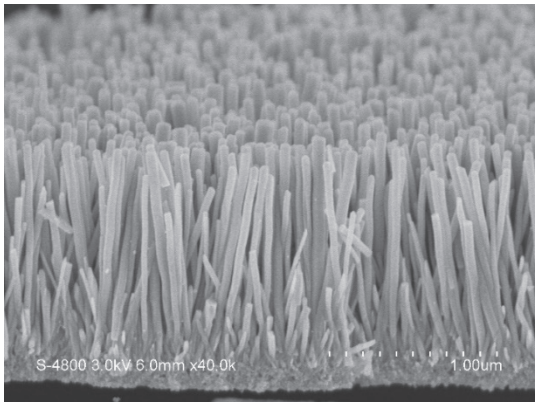

Fig. 5. Cross-sectional SEM image of CCZ nanowire arrays.

maintaining crystal symmetry. Figure 4(b) shows that the cross-sectional shape of CCZ nanowires approaches a circle. This morphology indicates that Co and Ca codoping suppresses the hexagonal formation. The spherical shape may be due to the introduction of dopants that create strains and defects in the lattice of ZnO nanowires. In addition, the cross-sectional SEM image of the CCZ nanowire array is shown in Fig. 5. The length of this vertical and aligned CCZ nanowire array is approximately 1 μm. To confirm the presence of Co and Ca elements in the prepared CCZ nanowire arrays, the elemental composition was qualitatively analyzed by energy dispersive X-ray spectroscopy (EDX) spectroscopy. Figure 6 shows the typical EDX spectrum of CCZ nanowires, showing different peaks corresponding to Zn, Co, Ca, and O mixed with these elements. Table 1 summarizes the EDX results for all samples.

3.4 Magnetic properties

The magnetic properties of undoped ZnO nanowires and CCZ nanowires were studied through VSM measurements at room temperature. The magnetization curves of the samples in Fig. 7 show the magnetic behaviors of ZnO and CCZ nanowires in different measurement directions (perpendicular and parallel to the nanowire array). In Fig. 7(a), the saturation magnetization (Ms) of the undoped ZnO nanowire under a vertical magnetic field is 0.22 emu/g, showing very weak magnetic properties. Ms of the CCZ nanowire in Fig. 7(b) is 0.46 emu/g, which is significantly higher than that of the undoped ZnO nanowire. CCZ nanowires exhibit ferromagnetic behavior at room temperature and have a clear hysteresis loop. This suggests that the incorporation of Co and Ca into the ZnO lattice introduces magnetic ordering, resulting in

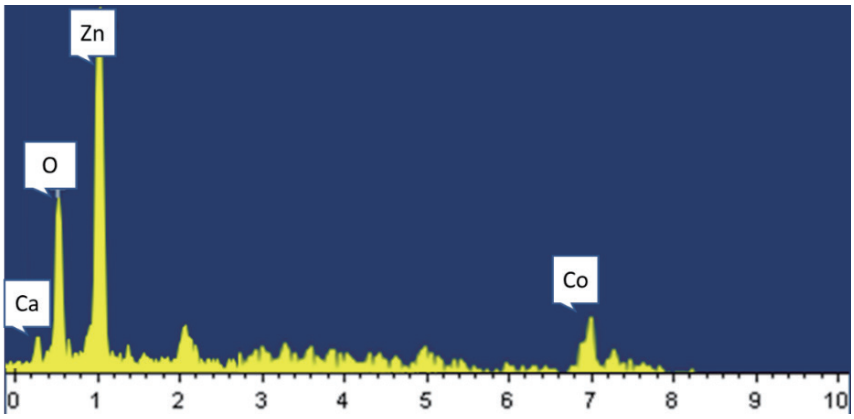

Fig. 6. (Color online) EDX spectrum of CCZ sample.

Table 1
EDX results of undoped ZnO nanowire and CCZ nanowire.

Samples	Element	Weight (%)	Atomic (%)
Undoped ZnO nanowire	Zn	80.8	50.6
	O	19.2	49.4
CCZ nanowire	Zn	77.4	44.5
	O	18.1	49.4
	Co	2.1	2.9
	Ca	2.4	3.2

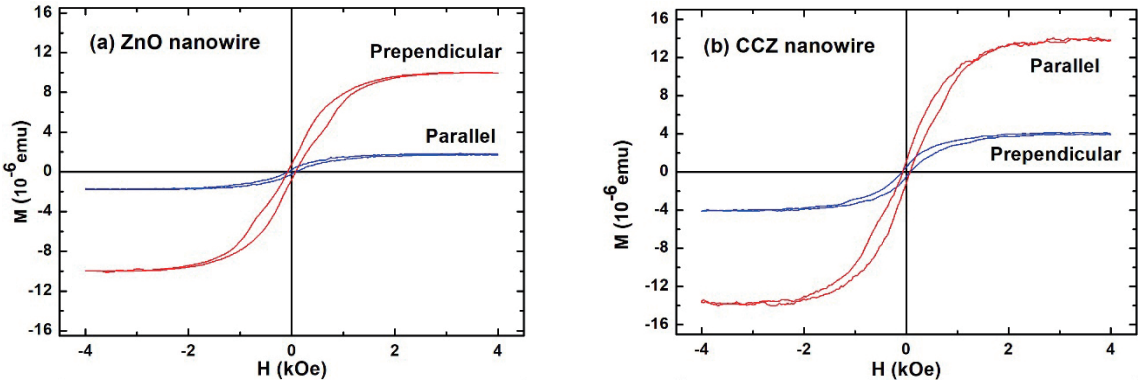

Fig. 7. (Color online) Magnetization curves measured at room temperature for (a) ZnO nanowires and (b) CCZ nanowires.

the observed ferromagnetic properties. This enhanced magnetization may be attributable to the contribution of the interaction between the local magnetic moments generated by the substitution of Co^{2+} ions for Zn^{2+} ions in the ZnO lattice to the overall magnetic response of the nanowires. In addition, the magnetization curves measured under magnetic fields applied perpendicular to

the nanowire array and parallel to the nanowire array show clears differences. Magnetization measured in the perpendicular direction exhibits higher coercivity and remanence than that measured in the parallel direction. This magnetic anisotropy suggests that the arrangement and shape of the nanowires, as well as their aspect ratio, play an important role in the magnetic behavior. The higher coercivity in the vertical direction can be attributed to the shape anisotropy of the nanowires, which makes it more difficult for the magnetic moment to reorient along the long axis of the nanowires when a magnetic field is applied perpendicular to the array.

3.5 Optical properties

The photoluminescence spectra (Fig. 8) of undoped ZnO nanowires and CCZ nanowires were measured at room temperature with an excitation wavelength of 325 nm . The photoluminescence spectrum of undoped ZnO nanowires exhibits a significant near-band edge (NBE) UV emission peak near 374 nm. This emission is attributed to the radiative recombination of excitons. The sharp NBE peak shows the high crystalline quality of undoped ZnO nanowires with minimal defects affecting emission. Furthermore, a broad and relatively weak green emission is observed at around 520 nm, which is attributed to deep defects such as oxygen vacancies or zinc interstitials in the ZnO lattice. The low intensity of green emission indicates that undoped ZnO nanowires have fewer inherent defects. Compared with undoped ZnO nanowires, the intensity of the UV emission peak at 374 nm of the CCZ nanowires is reduced, showing that Co and Ca dopants introduce additional nonradiative recombination centers and reduce the exciton recombination efficiency. This reduction in UV emission intensity is consistent with previous reports in which dopants or defects act as quenching centers for exciton emission.[27] The enhancement of green emission in the CCZ nanowires suggests that Co and Ca doping induce additional defect states within the ZnO lattice, such as increased oxygen vacancies.

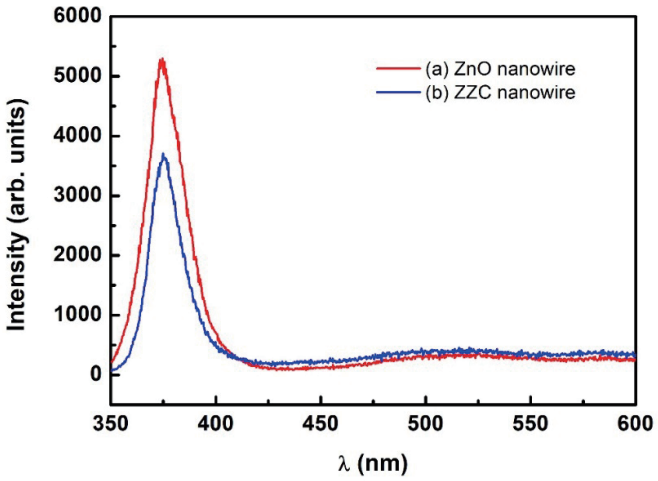

Fig. 8. (Color online) Photoluminescence spectra of (a) ZnO nanowire and (b) CCZ nanowire arrays at room temperature with an excitation wavelength at 325 nm.

4. Conclusions

In this study, the CCZ nanowire arrays were successfully synthesized on a silicon substrate by a hydrothermal method. The structural analysis using XRD confirmed the successful incorporation of Co and Ca dopants into the ZnO lattice. The results of magnetic measurements show that the magnetism of CCZ nanowires is significantly enhanced, with a saturation magnetization of 0.46 emu/g, whereas the saturation magnetization of undoped ZnO nanowires is only 0.22 emu/g. In addition, the magnetic anisotropy properties of CCZ nanowires have potential applications in spintronic devices and magnetic sensors. Photoluminescence analysis showed that the optical properties of CCZ nanowires changed significantly. The intensity of the UV emission decreased, and a significant enhancement of the green emission was observed. This change is attributed to the increase in the number of oxygen vacancies and defect states caused by Co and Ca codoping. The results of this study are the enhanced magnetic properties and improved light emission properties of ZnO nanowires through Co and Ca codoping. Moreover, CCZ nanowires have the potential for application in magneto-optical devices, spintronic devices, and advanced optoelectronic systems.

Acknowledgments

This work was sponsored by the National Science Council of the Republic of China under Grant no. NSTC 113-2637-E-324-001.

References

1 S. Chen, X. Song, X. Song, and Y. Zhang: Opt. Mater. **157** (2024) 116308.
2 W. Xue, D. Liu, S. Liang, X. Ma, and Z. Zhu: Mater. Sci. Semicond. Process. **186** (2025) 109021.
3 F. Meng, G. Li, H. Ji, and Z. Yuan: Sens. Actuators, B **423** (2025) 136747.
4 X. Wei, X. Yang, Y. Guo, Y. Liu, L. Wang, Q. Wang, L. Cheng, and Z. Jiao: Appl. Surf. Sci. **678** (2024) 161138.
5 Boukhoubza, M. Achehboune, I. Derkaoui, M. M. Apostol, M. Basyooni, M. Khenfouch, L. Nedelcu, I. Enculescu, and E. Matei: J. Alloys Compd. **976** (2024) 173109.
6 X. Dong, J. Deng, M. Ge, S. Lu, and Q. Zhu: Chem. Phys. Lett. **833** (2023) 140950.
7 M. Chakraborty, E. S. Kadir, M. Pradhan, M. Kangsabanik, and S. De, R.N. Gayen: Opt. Mater. **148** (2024) 114976.
8 W. Y. Chen, J. C. Lee, H. P. Hsu, Y. and F. Wu: Proc. Eng. Technol. Innov. **4** (2016) 16.
9 L. Li, Y. Xu, Y. Peng, J. Fan, H. Zhang, L. Jin, Y. Zou, and X. Ma: J. Lumin. **268** (2024) 120399.
10 X. Chen, Y. Ouyang, T. Liu, C. Zhang, S. Huang, H. Shang, H. Lin, S. Zhao, and Y. Shen: Vacuum **219** (2024) 112742.
11 A. Ievtushenko, V. Karpyna, L. Myroniuk, D. Myroniuk, L. Petrosian, O. Olifan, O. Kolomys, and V. Strelchuk: Chem. Phys. Lett. **857** (2024) 141720.
12 M. H. Rezoug, C. Zegadi, A. Nouri, N.-E. Hamdadou, and M. Guezzoul: Opt. Mater. **157** (2024) 116272.
13 N. A. Raship, S. N. M. Tawil, K. Ismail, and N. Nayan: Opt. Mater. **157** (2024) 116248.
14 V. Amrute, Monika, K. K. Supin, M. Vasundhara, and A. Chanda: RSC Adv. **14** (2024) 32786.
15 L. H. Kathwate: Ceram. Int. **50** (2024) 48462.
16 J. S. P. K., M. Shah, and P. P. Pradyumnan: Opt. Mater. **157** (2024) 116283.
17 S. Ashok Kumar, T. Govindhan, K. Selvakumar, K. Yusuf, S. Mahalingam, T. H. Oh, S. Ramasundaram, and J. Kim: Mater. Sci. Semicond. Process. **186** (2025) 109052.
18 S. Debnath, D. Nath, and R. Das: Physica B **696** (2025) 416678.
19 S. Hussain, Z. Zada, A. Reshak, D. Ali, F. Ali, A. Malik, M. Haneef, T. Amin, A. Laref, and M. M. Ramli: Opt. Mater. **157** (2024) 116208.

20 H. Wang, H. Zhao, W. Liang, S. Fan, and J. Kang: Mater. Sci. Semicond. Process. **133** (2021) 105880.
21 D. Ilager, N. P. Shetti, R. S. Malladi, N. S. Shetty, K. R. Reddy, and T. M. Aminabhavi: J. Mol. Liq. **322** (2021) 114552.
22 S. H. Zyoud and A. F. Omar: Sens. Actuators, A **379** (2024) 115971.
23 Y. Slimani, A. Khan, R. Sivakumar, M. Nawaz, and A. Thakur: J. Mol. Struct. **1322** (2025) 140366.
24 U. Javed, H.A. Sohail, A. Nazneen, M. Atif, G. M. Mustafa, and M. I. Khan: Solid State Commun. **390** (2024) 115616.
25 A. Bembibre, M. Benamara, M. Hjiri, E. Gómez, H. R. Alamri, R. Dhahri, and A. Serrà: Chem. Eng. J. **427** (2022) 132006.
26 A. I. Istrate, F. Nastase, I. Mihalache, F. Comanescu, R. Gavrila, O. Tutunaru, C. Romanitan, V. Tucureanu, M. Nedelcu, and R. Müller: J. Sol-Gel Sci. Technol. **92** (2019) 585.
27 S. N. Q. A. Abd Aziz, S. Y. Pung, Z. Lockman, and N. A. Hamzah: Adv. Mater. Res. **858** (2014) 151.